Thermalization of photoexcited carriers in two-dimensional transition metal dichalcogenides and internal quantum efficiency of van der Waals heterostructures

D. Yadav, M. Trushin, Fabian Pauly

Angaben zur Veröffentlichung / Publication details:

Yadav, D., M. Trushin, and Fabian Pauly. 2020. "Thermalization of photoexcited carriers in two-dimensional transition metal dichalcogenides and internal quantum efficiency of van der Waals heterostructures." *Physical Review Research* 2: 043051. https://doi.org/10.1103/PhysRevResearch.2.043051.

Thermalization of photoexcited carriers in two-dimensional transition metal dichalcogenides and internal quantum efficiency of van der Waals heterostructures

Dinesh Yadav,[1,2,*] Maxim Trushin,[3] and Fabian Pauly[1,2,*]

[1]*Okinawa Institute of Science and Technology Graduate University, Onna-son, Okinawa 904-0495, Japan*

[2]*Department of Physics, University of Konstanz, 78457 Konstanz, Germany*

[3]*Centre for Advanced 2D Materials, National University of Singapore, 6 Science Drive 2, Singapore 117546*

(Received 17 December 2019; revised 22 August 2020; accepted 16 September 2020; published 9 October 2020)

Van der Waals semiconductor heterostructures could be a platform to harness hot photoexcited carriers in the next generation of optoelectronic and photovoltaic devices. The internal quantum efficiency of hot-carrier devices is determined by the relation between photocarrier extraction and thermalization rates. Using *ab initio* methods we show that the photocarrier thermalization time in single-layer transition metal dichalcogenides strongly depends on the peculiarities of the phonon spectrum and the electronic spin-orbit coupling. In detail, the lifted spin degeneracy in the valence band suppresses the hole scattering on acoustic phonons, slowing down the thermalization of holes by one order of magnitude as compared with electrons. Moreover, the hole thermalization time behaves differently in MoS_2 and WSe_2 because spin-orbit interactions differ in these seemingly similar materials. We predict that the internal quantum efficiency of a tunneling van der Waals semiconductor heterostructure depends qualitatively on whether MoS_2 or WSe_2 is used.

DOI: 10.1103/PhysRevResearch.2.043051

I. INTRODUCTION

Utilizing high-energy carriers in photovoltaic devices could improve light-to-energy conversion efficiencies [1]. Despite recent progress with hot-carrier generation and injection in plasmonic nanostructures [2], the conventional semiconductor solar cells still demonstrate a superior efficiency without need for nanoscale fabrication. Alternative approaches to the problem either facilitate hot-electron transfer, e.g., from a chemically modified surface of lead selenide to titanium oxide [3], or extend photocarrier lifetimes, e.g., in some perovskites [4,5]. Van der Waals (vdW) semiconductor heterostructures formed from atomically thin two-dimensional (2D) crystals [6] might represent a suitable platform to take advantage of both phenomena, i.e., ultrafast photocarrier extraction and slow photocarrier thermalization.

The possibility to assemble vdW heterostructures layer by layer enables to tune electron transfer across interfaces in the out-of-plane dimension. This interlayer charge transfer directly competes with intralayer photocarrier thermalization. The scheme has first been realized in a graphene–boron-nitride–graphene vdW heterostructure [7], where the interlayer tunneling time ranges from 1 fs to 1 ps depending on bias voltage. Since the photocarrier thermalization time in graphene spans the interval between 10 fs and 10 ps depending on carrier concentration and excitation energy [8–13], there is a parameter range within which high-energy photocarrier extraction is feasible. Substituting graphene by a 2D transition metal dichalcogenide (TMDC) in a stack [14–17] opens new perspectives thanks to the possibility to create a diode configuration [18] and to realize stronger light-matter interactions [19]. There are already several reports on the fabrication of TMDC-based vdW heterostructures and their optoelectronic properties [20–22]. The high-energy photocarriers can be filtered out of a 2D semiconductor by means of a boron-nitride layer that constitutes a barrier for thermalized electrons and holes with low energy [21,22]. Since the photocarrier thermalization time is sensitive to the electron and phonon spectra of each semiconductor, it is important to compare this thermalization time with the interlayer tunneling time: The high-energy photocarrier transport may not be feasible if the former is too short. The relevant processes are sketched in Fig. 1. Note that we do not distinguish between the terms "hot" or "high-energy" carriers, but use them interchangeably.

Light-matter interaction in 2D TMDCs has recently been explored in time-resolved photoluminescence and transient absorption spectroscopy experiments using either linearly or circularly polarized light targeting exciton and carrier dynamics [23–38]. Experimental and theoretical studies of 2D TMDCs have largely focused on bound states for excitation energies below the electronic band gap, reporting exciton lifetimes [28,29,39], excitonic linewidths and diffusion rates [37,38], exciton-exciton annihilation [26,27], and exciton surface defect trapping [25]. Valley-resolved carrier dynamics has also been investigated around the band edge, and long valley depolarization times starting from a few ps for MoS_2 [24,29] to a few ns for WSe_2 [31–33] have been measured.

*Present address: Institute of Physics, University of Augsburg, 86135 Augsburg, Germany.

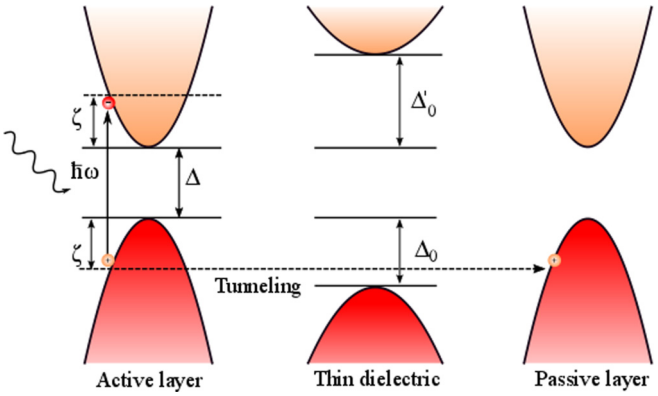

FIG. 1. Photocarrier excitation, thermalization, and tunneling in a semiconductor–dielectric–semiconductor vdW heterostructure. A weak bias (not shown) is applied to create a current across the layers. The internal quantum efficiency is determined by the ratio between thermalization and tunneling rates. Here, we consider transport through the valence bands because of the longer thermalization time for photoexcited holes.

Free photoexcited carrier thermalization in 2D TMDCs, arising for excitations above the band gap, has been studied much less comprehensively [23,30,34–36,40]. *Ab initio* studies have shown that the carrier-carrier scattering is efficient far away from the band edges due to a quadratic increase of the available phase space [41,42]. For a clean sample with no defects, the interaction with phonons thus represents the most important nonradiative channel for thermalization and cooling of photoexcited carriers in the vicinity of the valence- and conduction-band edges [25,40,43] and requires a deeper understanding.

In what follows, we use an approach already applied successfully to bulk and 2D materials [13,42,44,45]. For instance, we have demonstrated in our recent work that phonon emission by photocarriers in graphene is strongly suppressed at low excess energies of about 100 meV [13]. This phenomenon occurs because of high optical phonon frequencies due to strong carbon-carbon bonding and has been observed experimentally as a thermalization bottleneck [10]. In the present work we study the influence of spin-orbit coupling (SOC) on photocarrier thermalization in single-layer TMDCs and additionally relate intralayer thermalization rates to interlayer tunneling rates in vdW heterostructures, important for future optoelectronic devices with improved internal quantum efficiency (IQE). For this purpose we make use of density-functional theory (DFT) and density-functional perturbation theory (DFPT) to determine the electronic and phononic spectra of two 2D TMDC representatives, namely, MoS_2 and WSe_2. Furthermore, we compute band- and momentum-dependent scattering rates $\tau_{n\mathbf{k}}^{-1}$ for a given electronic band n and wave vector $\mathbf{k}$. Applying the Boltzmann equation in the relaxation-time approximation (RTA) we extract the total thermalization time τ_{th} as a function of excess energy and temperature. In our parameter-free *ab initio* modeling, we take relativistic SOC and all the acoustical and optical phonon branches in the first Brillouin zone (BZ) into account to provide a reliable description of electron-phonon scattering events. We show that photocarrier thermalization is slowed down by SOC-induced band splitting near valence-band maxima and conduction-band minima. Similar to interlayer transport, the thermalization occurs faster for photocarriers excited farther away from the band edges. We find, however, that the hole thermalization rate increases with excess energy in MoS_2 much more rapidly than in WSe_2. We therefore expect that the IQE of the tunneling device shown in Fig. 1 will strongly depend on whether MoS_2 or WSe_2 is employed.

II. THEORETICAL METHODS

A. *Ab initio* approach for electronic and phononic properties

We determine electronic and phononic properties of MoS_2 and WSe_2 monolayers by using DFT within the local density approximation (LDA) as implemented in QUANTUM ESPRESSO [46]. Six outermost electrons of each transition metal (Mo, W) and chalcogen (S, Se) are treated explicitly as valence electrons, while the remaining core electrons are included through norm-conserving Troullier-Martins pseudopotentials with relativistic corrections [47,48]. We employ a plane-wave basis set with a kinetic-energy cutoff of 70 Ry and a charge-density cutoff of 280 Ry. Unit cells of MoS_2 and WSe_2 monolayers are optimized with the help of the Broyden-Fletcher-Goldfarb-Shanno algorithm, neglecting SOC until the net force on atoms is less than 10^{-6} Ry/a.u. and total-energy changes are below 10^{-8} Ry. The monolayers are placed in a cell with a vacuum that separates periodic images by 18 Å to avoid artificial interactions in the out-of-plane direction. We find only small changes in the lattice constants, when considering SOC, which justifies its omission in the geometrical relaxation step. After geometry optimization we calculate the electronic ground-state density for the same structure with and without SOC, sampling the BZ with a $45 \times 45 \times 1$ Γ-centered $\mathbf{k}$ grid. We evaluate the phonon dispersion of MoS_2 and WSe_2 monolayers through DFPT [49] with and without SOC, employing a $12 \times 12 \times 1$ $\mathbf{q}$ grid to obtain phonon dynamical matrices. Next we construct localized Wannier functions from plane-wave eigenfunctions. By using the Wannier function interpolation scheme, we obtain electronic eigenenergies, dynamical matrices, and electron-phonon matrix elements on desired grids in the BZ [50–52].

After structural relaxation, the in-plane lattice constants $|\mathbf{a}|$ for MoS_2 and WSe_2 monolayers turn out to be 3.16 and 3.27 Å, respectively, which is in good agreement with experiment and previous *ab initio* calculations [53,54]. The electronic band structure is displayed in Figs. 2(a) and 2(b). We find a direct quasiparticle band gap of 1.74 eV at the K point in the BZ for MoS_2, while WSe_2 exhibits an indirect gap of 1.44 eV with the valence-band maximum at the K point and the conduction-band minimum located on the Γ-K direction. As DFT is known to underestimate band gaps, we apply a rigid shift to the unoccupied conduction bands to arrive at values of 2.82 and 2.42 eV for MoS_2 and WSe_2, respectively, which are consistent with the *GW* approximation [55,56]. This shift modifies the band-gap values but does not affect the time evolution of the hot carriers, to be discussed later. This assumption is valid because the electronic band gap is much larger than the highest phonon energy, and electrons and holes thus thermalize independently. Figures 2(a) and 2(b)

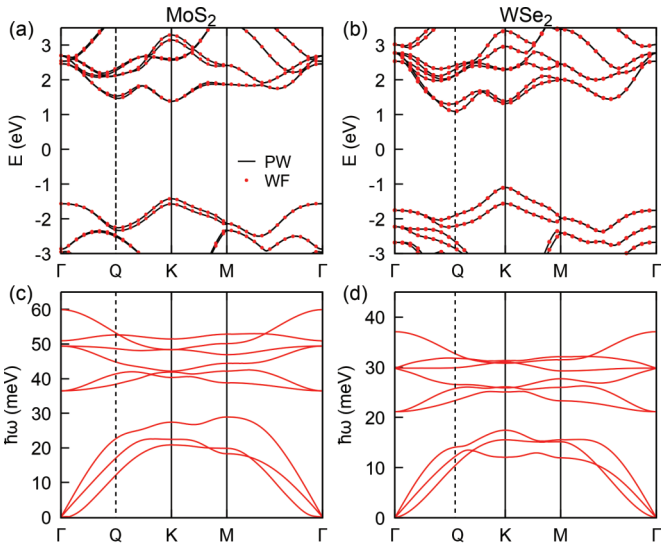

FIG. 2. Electronic band structure for monolayer (a) MoS_2 and (b) WSe_2, calculated with plane-wave (PW) and Wannier function (WF) basis sets. Phonon band structure for monolayer (c) MoS_2 and (d) WSe_2. Both electronic and phononic band structures take the relativistic SOC into account.

furthermore show that the Wannier-function-interpolated band structure matches exactly with the band structure determined with the plane-wave basis, confirming the high quality of the localized basis set. The spin splittings at the valence-band maxima of MoS_2 and WSe_2 at K amount to 151 meV and 464 meV, respectively. The lowest conduction band of WSe_2 exhibits spin-orbit splittings of 70 meV at the K point and 200 meV at the Q point, which we define as the minimum along the Γ-K direction [41,57], see Fig. 2. The corresponding splittings for the conduction band of MoS_2 are comparatively smaller with 3 meV at K and 70 meV at Q. Due to three atoms in the unit cell, MoS_2 and WSe_2 feature three acoustical and six optical modes of vibration, as is visible from the phononic band structure in Figs. 2(c) and 2(d). The highest frequencies of 60 and 37 meV for MoS_2 and WSe_2 monolayers occur at the Γ point, respectively, and these values agree with previously reported ones [58,59]. An energy gap separates acoustical and optical branches, which will be exploited in the analysis of thermalization times further below. We have verified that the use of the truncated Coulomb interaction does not introduce any major changes in the electronic and phononic band structures of Fig. 2 [60].

Having determined electronic and phononic band structures, we evaluate the electronic self-energy $\Sigma_{n\mathbf{k}}(T)$ in the lowest order of the electron-phonon interaction for band n and wave vector $\mathbf{k}$ at temperature T by using the EPW code [52]. It is expressed as

$$\Sigma_{n\mathbf{k}}(T) = \sum_{m,p} \int_{\mathrm{BZ}} \frac{d^3q}{\Omega_{\mathrm{BZ}}} |g_{mn,p}(\mathbf{k},\mathbf{q})|^2 \left[\frac{N_{p\mathbf{q}}(T) + f^{(0)}_{m\mathbf{k}+\mathbf{q}}(T)}{\varepsilon_{n\mathbf{k}} - (\varepsilon_{m\mathbf{k}+\mathbf{q}} - \varepsilon_{\mathrm{F}}) + \hbar\omega_{p\mathbf{q}} + i\eta} + \frac{N_{p\mathbf{q}}(T) + 1 - f^{(0)}_{m\mathbf{k}+\mathbf{q}}(T)}{\varepsilon_{n\mathbf{k}} - (\varepsilon_{m\mathbf{k}+\mathbf{q}} - \varepsilon_{\mathrm{F}}) - \hbar\omega_{p\mathbf{q}} + i\eta} \right]. \quad (1)$$

Here, $\hbar\omega_{p\mathbf{q}}$ is the energy of the phonon of branch p at wave vector $\mathbf{q}$, $\varepsilon_{\mathrm{F}} = 0$ is the Fermi energy, $f^{(0)}_{n\mathbf{k}}(T) = 1/[\exp(\frac{\varepsilon_{n\mathbf{k}} - \varepsilon_{\mathrm{F}}}{k_{\mathrm{B}}T}) + 1]$ is the Fermi-Dirac distribution, $N_{p\mathbf{q}}(T) = 1/[\exp(\frac{\hbar\omega_{p\mathbf{q}}}{k_{\mathrm{B}}T}) - 1]$ is the Bose function, Ω_{BZ} is the volume of the BZ, and $\eta = 20$ meV is a small broadening parameter. The electron-phonon matrix elements are defined as [52]

$$g_{mn,p}(\mathbf{k},\mathbf{q}) = \frac{1}{\sqrt{2\omega_{p\mathbf{q}}}} \langle m\mathbf{k}+\mathbf{q} | \partial_{p\mathbf{q}} V | n\mathbf{k} \rangle, \quad (2)$$

describing transitions between the Kohn-Sham states $|n\mathbf{k}\rangle$ and $|m\mathbf{k}+\mathbf{q}\rangle$ mediated by the phonon $p\mathbf{q}$. Here, $\partial_{p\mathbf{q}}V$ is the derivative of the self-consistent Kohn-Sham potential with respect to displacements of nuclei along the phonon mode $p\mathbf{q}$. The first term in the brackets of Eq. (1) arises from the absorption of phonons and the second one from their emission. To compute $\Sigma_{n\mathbf{k}}(T)$, we interpolate electronic and vibrational states on fine $300 \times 300 \times 1$ $\mathbf{k}$ and $\mathbf{q}$ grids, which we find sufficient to accurately map the first BZ and to converge the integral over $\mathbf{q}$.

Our model makes the following assumptions: (i) Changes induced by the electron-phonon coupling in the electronic wave functions and phonon dynamical matrices are small and can be neglected [52]. (ii) Similarly, renormalization of phonon frequencies due to anharmonic effects is ignored [61]. (iii) Electron and phonon baths are at the same temperature T all the time. The electron-phonon scattering time for a carrier in the state $|n\mathbf{k}\rangle$ is then given by

$$\tau_{n\mathbf{k}}(T) = \frac{\hbar}{2\mathrm{Im}[\Sigma_{n\mathbf{k}}(T)]}. \quad (3)$$

Conversely, $\mathrm{Im}[\Sigma_{n\mathbf{k}}(T)]$ is proportional to the electron-phonon scattering rate $\tau_{n\mathbf{k}}(T)^{-1}$.

B. Time-evolution of excited charge carriers

We determine the time evolution of the electronic occupation $f_{n\mathbf{k}}(t,T)$ by using the Boltzmann equation in the RTA:

$$\frac{df_{n\mathbf{k}}(t,T)}{dt} = -\frac{f_{n\mathbf{k}}(t,T) - f^{\mathrm{th}}_{n\mathbf{k}}(T)}{\tau_{n\mathbf{k}}(T)}, \quad (4)$$

which has the solution

$$f_{n\mathbf{k}}(t,T) = f^{\mathrm{th}}_{n\mathbf{k}}(T) + e^{-\frac{t}{\tau_{n\mathbf{k}}(T)}} \left[f_{n\mathbf{k}}(0,T) - f^{\mathrm{th}}_{n\mathbf{k}}(T) \right]. \quad (5)$$

Here, $f^{\mathrm{th}}_{n\mathbf{k}}(T)$ is the thermalized Fermi distribution at $t \to \infty$, where the quasi-Fermi level is chosen to reproduce the number of carriers initially present. The description through the Boltzmann equation (4) is valid only, if the number of carriers excited at $t = 0$ represents a weak perturbation. The RTA relaxes an excited charge carrier directly to the thermalized state, omitting all intermediate relaxation steps between the initial nonequilibrium and final relaxed occupation.

We start with a hot-carrier occupation $f_{n\mathbf{k}}(0,T)$ that consists of the sum of a Fermi-Dirac distribution $f^{(0)}_{n\mathbf{k}}(T)$ at temperature T and a Gaussian peak centered at energy $+\zeta + \Delta/2$ or $-\zeta - \Delta/2$ for electrons or holes, respectively, see also Fig. 1, as

$$f_{n\mathbf{k}}(0,T) = f^{(0)}_{n\mathbf{k}}(T) - \frac{\lambda_\mathrm{h}}{\sqrt{2\pi\sigma^2}} e^{\frac{(\varepsilon_{n\mathbf{k}}+\zeta+\Delta/2)^2}{2\sigma^2}}, \quad \varepsilon_{n\mathbf{k}} < \varepsilon_\mathrm{F},$$
$$f_{n\mathbf{k}}(0,T) = f^{(0)}_{n\mathbf{k}}(T) + \frac{\lambda_\mathrm{e}}{\sqrt{2\pi\sigma^2}} e^{\frac{(\varepsilon_{n\mathbf{k}}-\zeta-\Delta/2)^2}{2\sigma^2}}, \quad \varepsilon_{n\mathbf{k}} \geqslant \varepsilon_\mathrm{F}. \tag{6}$$

In the expressions, Δ is the electronic energy gap of the considered material, and the Gaussian distribution uses a small energy broadening $\sigma = 8.47$ meV. Since valence and conduction bands feature an energy-dependent density of states (DOS), the parameters λ_e and λ_h are adjusted such that the same number of photoexcited carriers is present at any excess energy ζ. In particular, we define them in terms of the energy-, time- and temperature-dependent population

$$P(E,t,T) = \sum_{n\mathbf{k}} \delta(E-\varepsilon_{n\mathbf{k}}) \times \begin{cases} [1-f_{n\mathbf{k}}(t,T)], & E < \varepsilon_\mathrm{F} \\ f_{n\mathbf{k}}(t,T), & E \geqslant \varepsilon_\mathrm{F} \end{cases} \tag{7}$$

as

$$\lambda_\mathrm{e} = \frac{n_\mathrm{e} A}{\int_{\varepsilon_\mathrm{F}}^{\varepsilon_\mathrm{max}} P(E,t=0,T)dE},$$
$$\lambda_\mathrm{h} = \frac{n_\mathrm{h} A}{\int_{-\varepsilon_\mathrm{max}}^{\varepsilon_\mathrm{F}} P(E,t=0,T)dE}, \tag{8}$$

where n_e and n_h are the photoexcited electron and hole areal densities, respectively, which we choose to be equal ($n_\mathrm{e} = n_\mathrm{h}$), and A is the area of the unit cell of the respective monolayer. We integrate the population with a sufficiently large $\varepsilon_\mathrm{max} = 3$ eV symmetrically around the Fermi energy $\varepsilon_\mathrm{F} = 0$ (see also Fig. 2).

We define the thermalization time τ_th as

$$\frac{P(\zeta,\tau_\mathrm{th},T)}{P(\zeta,0,T)} = \frac{1}{e}. \tag{9}$$

In our numerical calculations, we approximate the δ function in Eq. (7) by a narrow Gaussian with a width of 20 meV. We focus on electronic excitations far enough above the quasi-Fermi levels such that the finite width does not affect τ_th.

C. Interlayer charge transport

Having the thermalization time at hand, we need a reference timescale to see whether high-energy photoexcited carriers can contribute to interlayer charge transport in vdW heterostructures, as sketched in Fig. 1. An accurate calculation of the interlayer transport time is a challenging task, because the carrier motion across interfaces is subject to multiple uncontrolled effects, e.g., interfacial roughness and impurity scattering. These effects may vary even within the same batch of samples, let alone the use of different 2D materials. In what follows, we employ a concept based on the transmission coefficient for carriers tunneling through a barrier and the uncertainty relation between the photocarrier excess energy and lifetime [7]. The advantage of the approach is that we can straightforwardly relate the transmission probability of the photoexcited carriers to a measurable quantity, namely, the IQE.

Our starting point is the well-known transmission probability of carriers through a rectangular barrier of width d and height Δ_0 counted from the respective band edge, see Fig. 1. We assume the tunneling regime [7] so that the photocarrier excess energy is always below the barrier, $\zeta < \Delta_0$. Note that, according to the conventions used in this work, ζ and Δ_0 are both positive, even for holes. We assume that the in-plane photocarrier momentum is not conserved due to interfacial disorder, rendering the problem effectively one-dimensional. We must, however, change the physical meaning of the incident wave vector k_z. It does not describe propagating waves anymore but is related to the out-of-plane momentum uncertainty $\Delta p_z/\hbar$, which is of the order of the size of the first Brillouin zone for 2D conductors [62]. The approximations can formally be summarized as [7,63]

$$\mathcal{T}(\zeta) = \frac{4k_z^2\kappa^2}{\left(k_z^2+\kappa^2\right)^2 \sinh^2\kappa d + 4k_z^2\kappa^2} \tag{10}$$
$$\approx \frac{4k_z^2\kappa^2}{\left(k_z^2+\kappa^2\right)^2} e^{-2\kappa d}, \quad \kappa d \gg 1 \tag{11}$$
$$\approx \frac{4\kappa^2}{k_z^2} e^{-2\kappa d}, \quad k_z \gg \kappa \tag{12}$$
$$\approx 8\frac{\Delta_0-\zeta}{v_z\Delta p_z} \exp\left(-\frac{2d}{\hbar}\sqrt{2m(\Delta_0-\zeta)}\right). \tag{13}$$

In the last line, we have used the relations $\hbar\kappa = \sqrt{2m(\Delta_0-\zeta)}$ and $\hbar^2 k_z^2/m \approx v_z\Delta p_z$. Since the structure is aperiodic along the out-of-plane direction, the effective mass m of the quasiparticle moving across the interface equals the free-electron mass.

The probability for a given photoexcited carrier to get across the tunneling junction can be written as the ratio between thermalization and tunneling times, $\mathcal{T} \approx \tau_\mathrm{th}/\tau_\mathrm{tun}$ with $\tau_\mathrm{th} \ll \tau_\mathrm{tun}$. The tunneling time is obviously longer for thicker barriers, and the probability is thus lower. The thermalization time can also be seen as the lifetime for a carrier to be in a photoexcited state. Importantly, there is a relation between the quasiparticle velocity, momentum uncertainty, and lifetime [62,63], $v_z\Delta p_z \approx \hbar/\tau_\mathrm{th}$. By making this substitution in the denominator of Eq. (13), it becomes obvious that the numerator is the tunneling rate that we are looking for. To estimate τ_tun we neglect multipliers of the order of unity. Hence, the tunneling time can be written as

$$\frac{1}{\tau_\mathrm{tun}} \approx \frac{\Delta_0-\zeta}{\hbar} \exp\left(-\frac{2d}{\hbar}\sqrt{2m(\Delta_0-\zeta)}\right). \tag{14}$$

Equation (14) is somewhat similar to the transport time formula for a triangular barrier, employed previously [7,64] to describe electron tunneling in the Fowler-Nordheim regime. In our case, we assume a low bias and a thin barrier such that the voltage does not appear in τ_tun explicitly, but it may influence Δ_0. As we need τ_tun solely for comparison with τ_th by the order of magnitude, we estimate it roughly for $\Delta_0 \approx 1$ eV and $d \approx 1$ nm. The interlayer transport time then ranges between 100 fs to 10 ps, depending on the excess energy. To gain a substantial photocurrent, the interlayer transport must

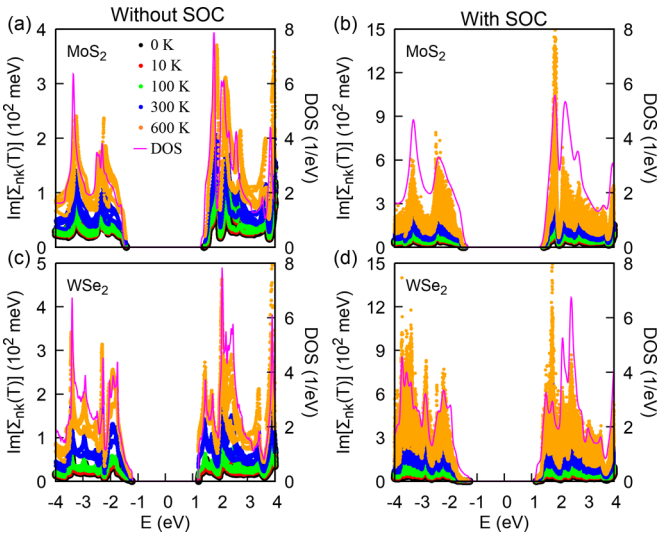

FIG. 3. Imaginary part of the electron-phonon self-energy as a function of energy calculated for different temperatures without and with SOC for (a), (b) MoS_2 and (c), (d) WSe_2 monolayers. The DOS is also shown in each panel by a solid line. Note that the scatter plots of $\mathrm{Im}[\Sigma_{n\mathbf{k}}]$ at different temperatures are overlayed, meaning that higher T hide some of the features present at lower T.

not be too slow as compared with thermalization. From the experimental point of view, the ratio $\tau_{\mathrm{th}}/\tau_{\mathrm{tun}}$ is nothing else but the IQE in the tunneling limit $\tau_{\mathrm{th}} \ll \tau_{\mathrm{tun}}$. In the following section we will further analyze τ_{th}, τ_{tun} and the ratio $\tau_{\mathrm{th}}/\tau_{\mathrm{tun}}$.

III. RESULTS

We start by discussing the imaginary part of the self-energy, which is proportional to the electron-phonon scattering rate $\tau_{n\mathbf{k}}^{-1}$. Figure 3 shows $\mathrm{Im}[\Sigma_{n\mathbf{k}}]$ for MoS_2 and WSe_2 with and without SOC as a function of energy at different temperatures. The energy dependence of $\mathrm{Im}[\Sigma_{n\mathbf{k}}]$ follows that of the electronic DOS. This can be understood from Eq. (1), where the self-energy for state $|n\mathbf{k}\rangle$ is determined by a sum over all electronic states $|m\mathbf{k}+\mathbf{q}\rangle$. Considering that phonon energies are limited to below 60 meV for both materials, the sum essentially constitutes an integral over electronic states in the vicinity of $\varepsilon_{n\mathbf{k}}$, which is proportional to the electronic DOS. SOC reshapes the electronic band structure by splitting spin-degenerate states. On the rather large energy scales shown in Fig. 3, comprising excess energies of up to 3 eV, we find that this can increase the imaginary part of the self-energy as compared with the case without SOC. $\mathrm{Im}[\Sigma_{n\mathbf{k}}]$ generally grows with increasing temperature. While at low T only phonon emission is allowed, at high T carriers can scatter by both phonon emission and absorption. Let us point out that we have verified that the polar-optical coupling with longitudinal optical phonons [65,66], the Fröhlich interaction, does not modify the imaginary part of the self-energy significantly.

More relevant to us are the effects of SOC around the band edges. Comparing scattering times with and without SOC in Fig. 4, we observe that the $\tau_{n\mathbf{k}}$ are strongly increased by SOC for holes of both MoS_2 and WSe_2 and electrons of WSe_2. The electron states of MoS_2, on the other hand, are basically unaffected. The large increase of $\tau_{n\mathbf{k}}$ correlates with

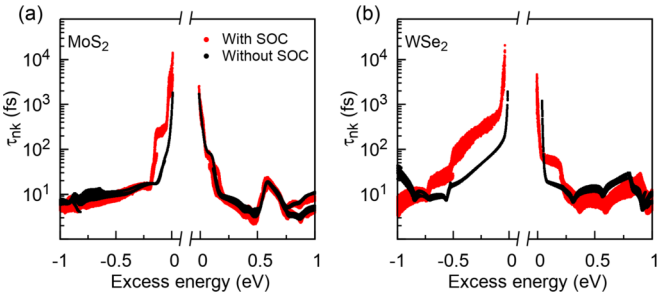

FIG. 4. Scattering times as a function of excess energy with and without SOC for (a) MoS_2 and (b) WSe_2 at $T = 0$ K.

a large spin-orbit splitting of the corresponding valence- and conduction-band states in Fig. 2. Let us point out that similar calculations of $\tau_{n\mathbf{k}}$ have already been presented by Ciccarino *et al.* [41]. These authors have assigned the increased scattering times around the valence-band edges to the suppression of intervalley scattering between K and K′ and a corresponding spin-valley locking [41]. However, they claimed that there would be no electron-lifetime enhancement compared with the case without SOC, although they report a clear spin-orbit splitting of the lowest conduction band for WSe_2. Sohier *et al.* [57] analyzed the electron-phonon matrix elements without SOC for the conduction band edge of various electron-doped TMDCs. For WSe_2 they found nonvanishing matrix elements in momentum space between K and K′ points as well as K and Q. Although we do not provide a momentum-resolved understanding here, we expect a similar kind of enhancement in electron lifetimes at the conduction-band edges, as explained in Ref. [41] for holes at the valence-band edges, if SOC leads to a substantial spin splitting and modifies the selection rules for electron-phonon couplings. Beside this aspect of electron lifetime enhancement, we go beyond Ref. [41] by calculating thermalization times with the Boltzmann equation for a range of excitation energies, by distinguishing the roles of acoustical and optical phonons in the scattering processes and by comparing thermalization to tunneling times in vdW heterostructures.

Typical densities of carriers excited in pump-probe experiments lie between 10^{11} to 10^{13} cm^{-2} [23,28,67]. We adjust our free parameters λ_e, λ_h of Eq. (6) such that we generate nonequilibrium populations corresponding to densities of 7×10^{12} cm^{-2} carriers in the valence and conduction bands for all the initial-state preparations throughout the paper. The time evolution of the occupation is then calculated by using Eq. (5) with the thermalized Fermi-Dirac distribution $f_{n\mathbf{k}}^{\mathrm{th}}$ centered at a quasi-Fermi level such that the density of 7×10^{12} cm^{-2} carriers is also present after thermalization. This assumption of a conserved number of carriers is valid because radiative recombination times of electron-hole pairs in MoS_2 and WSe_2 are of the order of a few ps [25,28,39]. They are thus much longer than the thermalization times that we report in the following.

Figure 5(a) shows the evolution of the hot-carrier population for MoS_2 at $T = 0$ K without SOC. In this case, thermalization times of electrons and holes are comparable. Upon introducing the SOC, it can be seen in Fig. 5(b) that the thermalization time of holes is increased, whereas it remains almost unchanged for electrons. WSe_2 follows the same

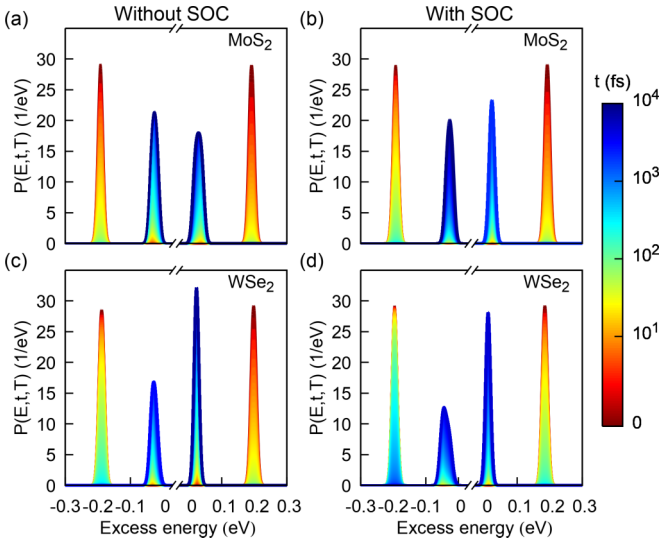

FIG. 5. Time evolution of photoexcited carriers with and without SOC in (a), (b) MoS_2 and (c), (d) WSe_2 monolayers at an excess energy of $\zeta = 0.2$ eV for $T = 0$ K. Initial and final photoexcited carrier populations correspond to a carrier density of 7×10^{12} cm^{-2}. Note that, due to the large spin-orbit splitting near the valence-band edge, the thermalized population is rather broad in panels (b) and (d), but the area under initial and final distributions remains constant.

trend as MoS_2, see Figs. 5(c) and 5(d), although lifetimes of electrons are also visibly increased by SOC. We attribute this behavior to the strong spin-orbit splitting of the valence band in both MoS_2 and WSe_2 and a comparatively smaller splitting of the conduction band in WSe_2.

The finite-energy separation between optical and acoustical branches, observed in Fig. 2, makes it possible to distinguish them in $\mathrm{Im}[\Sigma_{n\mathbf{k}}] = \mathrm{Im}[\Sigma_{n\mathbf{k}}]_{\mathrm{ac}} + \mathrm{Im}[\Sigma_{n\mathbf{k}}]_{\mathrm{op}}$ and consequently in $\tau_{\mathrm{th}}^{-1} = \tau_{\mathrm{th,ac}}^{-1} + \tau_{\mathrm{th,op}}^{-1}$. In Figs. 6 and 7 we show thermalization times determined by disregarding or considering SOC,

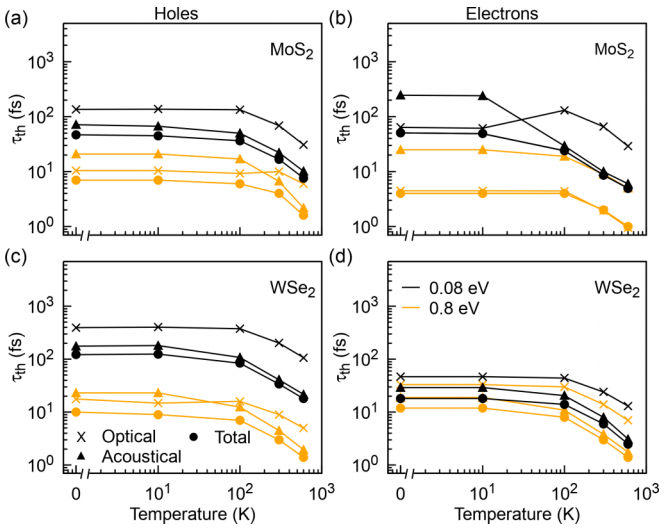

FIG. 6. Contributions of acoustical and optical phonons to the thermalization of hot holes (left) and hot electrons (right) in (a), (b) MoS_2 and (c), (d) WSe_2 monolayers at two different excess energies of $\zeta = 0.08$ and 0.8 eV, neglecting SOC.

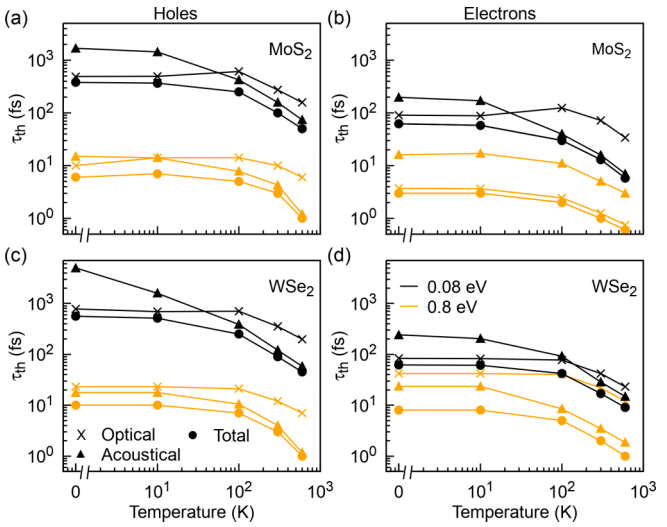

FIG. 7. Same as Fig. 6 but including SOC.

respectively. Beside the total thermalization time τ_{th} (•) we display $\tau_{\mathrm{th,ac}}$ (▲) and $\tau_{\mathrm{th,op}}$ (×), calculated by taking into account only acoustical or optical phonons. In Fig. 6 it can be seen that thermalization of electrons and holes at low temperatures near the band edges (see the low excess energy $\zeta = 0.08$ eV, which is still larger than the optical phonon energies) is typically dominated by low-energy acoustical phonons. The electrons of MoS_2 constitute an exception, since their thermalization is governed by optical phonons. With increasing temperature, acoustical phonons keep their dominant influence on τ_{th} or start to dominate the electron-phonon scattering at $T \gtrsim 100$ K for the electrons of MoS_2. Away from the band edges (see the high excess energy $\zeta = 0.8$ eV) a rather diverse picture arises, where both acoustical and optical contributions can define thermalization. Once SOC is introduced in Fig. 7, the contribution of acoustical phonons is strongly suppressed for low ζ and low T, while that of the optical phonons remains nearly unaffected. For this reason the thermalization of both electrons and holes at low temperatures is fully governed by optical phonons. With increasing temperature, acoustical phonons play an increasingly important role, and at $T \gtrsim 100$ K they define the decreasing behavior of τ_{th}. Altogether, the effects of SOC slow down thermalization near the band edges.

Let us note that, for excitations below optical phonon energies (not shown), i.e., below 30 and 20 meV for MoS_2 and WSe_2, respectively, and at low temperatures we observe that only acoustical phonons contribute to the thermalization, because there is no energy available for optical phonon emission. Total thermalization times then coincide with the acoustical relaxation times displayed in Figs. 6 and 7, and can be substantially enhanced.

We summarize the total thermalization time τ_{th} in Fig. 8 as a function of temperature for different excess energies. The dashed curves represent the thermalization time without SOC, and the solid curves include SOC. While SOC strongly increases the thermalization time at low T near the band edges, τ_{th} may also decrease [see for instance $\zeta =$ 0.8 eV in Fig. 8(d)] depending upon the band structure and electron-phonon couplings. For a fixed excess energy

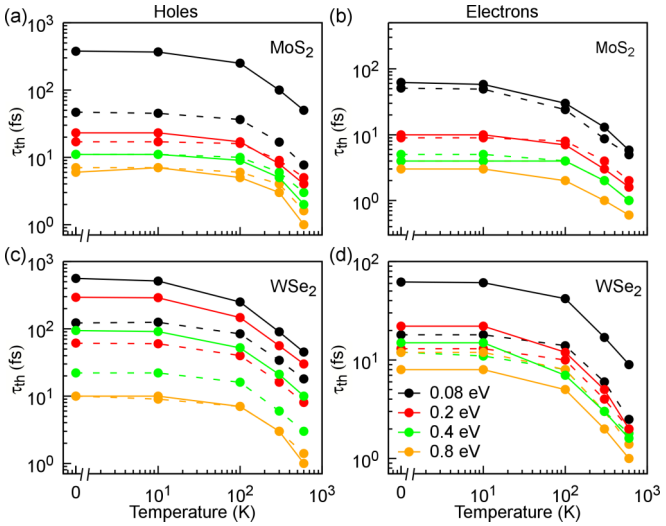

FIG. 8. Hot carrier thermalization times for holes (left) and electrons (right) in (a), (b) MoS_2 and (c), (d) WSe_2 monolayers at different excess energies ζ. Solid lines represent thermalization times with SOC and dashed lines those without SOC.

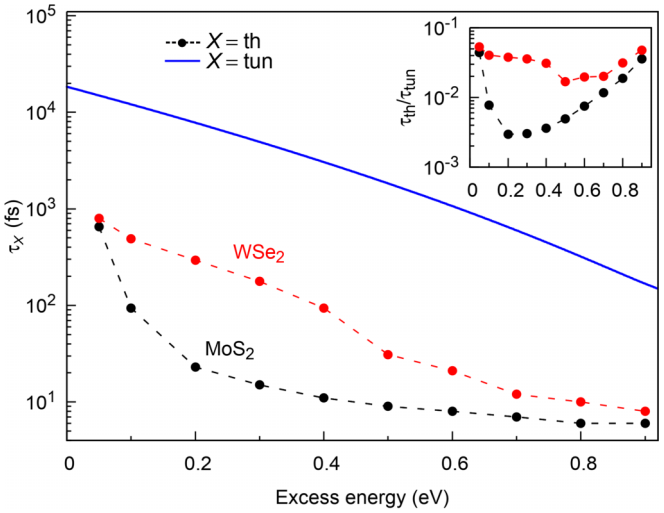

FIG. 9. Comparison of thermalization and tunneling times for holes in MoS_2 and WSe_2 heterostructures, see Fig. 1, as a function of excess energy ζ measured from the valence-band maxima. The inset shows the ratio τ_{th}/τ_{tun}. Thermalization times include the effect of SOC and are evaluated at $T = 0$ K.

the thermalization time generally decreases with increasing temperature, because more phonons are accessible to scatter on electrons and holes. The same trend has been reported in pump-probe experiments performed on five-layer MoS_2 [23], where the drop of τ_{th} has been observed for electrons at around $T = 300$ K. Figures 8(a) and 8(b) suggests that it occurs around 100 K for MoS_2 in our theory. It should, however, be emphasized that we study perfectly crystalline, free-standing layers in vacuum. The presence of a substrate, defects, and interlayer interactions thus complicates a comparison with the experimental results. A qualitative agreement is nevertheless achieved.

As visible in Fig. 8, free carriers near the band edges feature longer relaxation times as compared with those at higher excess energies. The reason is the lower electronic DOS available for scattering around the band edges. Caused by multiple valleys in the conduction band, see Figs. 2 and 3, electrons thermalize faster than holes in both MoS_2 and WSe_2. Due to the heavier elements composing WSe_2, the SOC-related splitting at both the valence- and conduction-band edges is larger than in MoS_2. This alters the thermalization time of both electrons and holes. However, electrons still thermalize one order of magnitude faster than holes around band edges. As a rule of thumb thermalization times around the band edges are increased as compared with the case without SOC as long as ζ is less than the spin-orbit-induced band splitting. In other words, there exists a direct correlation between thermalization-time enhancement and the size of the SOC. Considering regions more distant from the band edges, the effect of the SOC is quite complex, since it modifies electron-phonon couplings and hence the relaxation rates $\tau^{-1}_{n\mathbf{k}}$ (see also Fig. 3). We note that our calculated thermalization times of electrons in MoS_2 for $\zeta = 0.05$ eV amount to 63 and 36 fs at 10 and 100 K, respectively, which is of a similar magnitude as found in Ref. [36], where $\tau_{th} \approx 30$ fs at $T \approx 50$ K.

Since our calculations predict that holes thermalize more slowly than electrons in both MoS_2 and WSe_2, we focus on hole transport to discuss the IQE of the tunneling device presented in Fig. 1. The heterostructure that we have in mind thus consists of two single layers of 2D TMDCs at the outside, which are separated by a 1-nm-thick dielectric film that establishes a tunneling barrier Δ_0 of 1 eV to the valence-band maximum of the single layers. Figure 9 shows how the photoexcited hole thermalization time τ_{th} compares to the tunneling time τ_{tun} of Eq. (14) as a function of the excess energy ζ. Surprisingly, τ_{th} follows the same trend as τ_{tun} for WSe_2. The ratio τ_{th}/τ_{tun} thus depends only weakly on ζ, as is visible in the inset of Fig. 9. This suggests that the IQE of the vdW heterostructure stays rather constant with regard to increasing photocarrier excess energy. This contrasts with the case of MoS_2, where τ_{th} drops much faster than τ_{tun} when ζ increases. Hence, we expect that an analogous MoS_2-based tunneling device will demonstrate a pronounced decay in the IQE once the photocarriers are excited away from the band edges. Ultimately, our calculations trace back this effect to the larger SOC-induced valence-band splitting of WSe_2 as compared with MoS_2 in these otherwise similar materials, see Fig. 2. Thermalization times for MoS_2 and WSe_2 converge at higher excess energies, which exceed the band-edge-related SOC splitting.

IV. CONCLUSIONS

We have combined DFT with many-body perturbation theory to calculate scattering times of photoexcited carriers in MoS_2 and WSe_2 monolayers arising from electron-phonon interactions. Our model takes all of the phonon branches and their dispersion into account in the scattering processes and highlights the crucial influence of SOC on the thermalization time. In the relevant region near the band edges we find that the inclusion of SOC generally increases the thermalization times by up to an order of magnitude. Our analysis assigns this effect to a suppression of acoustical-phonon scattering, while thermalization by optical phonons remains basically

unaffected. In both monolayers electrons thermalize almost one order of magnitude faster than holes.

We have additionally estimated the tunneling time of a TMDC-based heterostructure by using an analytical model. The ratio of thermalization and tunneling times decreases weakly with photocarrier excess energy in WSe_2, whereas it drops quickly for MoS_2 when moving away from the valence-band maximum. Our calculations hence suggest that tunneling devices based on WSe_2 monolayers will have a higher internal quantum efficiency than MoS_2-based systems.

ACKNOWLEDGMENTS

The authors thank G. Eda for stimulating discussions. D.Y. and F.P. acknowledge financial support from the Carl Zeiss Foundation as well as the Collaborative Research Center (SFB) 767 of the German Research Foundation (DFG). M.T. acknowledges the Director's Senior Research Fellowship from the Centre for Advanced 2D Materials at the National University of Singapore (National Research Foundation Singapore Medium-Sized Centre Programme [R-723-000-001-281], Singapore Ministry of Education AcRF Tier 2 MOE2017-T2-2-140 [R-607-000-352-112], NUS Young Investigator Award [R-607-000-236-133]), and thanks the Okinawa Institute of Science and Technology for its hospitality during two visits of around one week each. Part of the numerical modeling was performed using the computational resources of the bwHPC program, namely the bwUniCluster and the JUSTUS HPC facility.

[1] J. Nelson, *The Physics of Solar Cells* (Imperial College Press, London, 2003).

[2] C. Clavero, Plasmon-induced hot-electron generation at nanoparticle/metal-oxide interfaces for photovoltaic and photocatalytic devices, Nat. Photonics **8**, 95 (2014).

[3] W. A. Tisdale, K. J. Williams, B. A. Timp, D. J. Norris, E. S. Aydil, and X.-Y. Zhu, Hot-electron transfer from semiconductor nanocrystals, Science **328**, 1543 (2010).

[4] H. Kawai, G. Giorgi, A. Marini, and K. Yamashita, The mechanism of slow hot-hole cooling in lead-iodide perovskite: First-principles calculation on carrier lifetime from electron-phonon interaction, Nano Lett. **15**, 3103 (2015).

[5] H.-H. Fang, S. Adjokatse, S. Shao, J. Even, and M. A. Loi, Long-lived hot-carrier light emission and large blue shift in formamidinium tin triiodide perovskites, Nat. Commun. **9**, 243 (2018).

[6] K. S. Novoselov, A. Mishchenko, A. Carvalho, and A. H. Castro Neto, 2D materials and van der Waals heterostructures, Science **353**, aac9439 (2016).

[7] Q. Ma, T. I. Andersen, N. L. Nair, N. M. Gabor, M. Massicotte, C. H. Lui, A. F. Young, W. Fang, K. Watanabe, T. Taniguchi, J. Kong, N. Gedik, F. H. L. Koppens, and P. Jarillo-Herrero, Tuning ultrafast electron thermalization pathways in a van der Waals heterostructure, Nat. Phys. **12**, 455 (2016).

[8] M. Mittendorff, T. Winzer, E. Malic, A. Knorr, C. Berger, W. A. de Heer, H. Schneider, M. Helm, and S. Winnerl, Anisotropy of excitation and relaxation of photogenerated charge carriers in graphene, Nano Lett. **14**, 1504 (2014).

[9] M. Trushin, A. Grupp, G. Soavi, A. Budweg, D. De Fazio, U. Sassi, A. Lombardo, A. C. Ferrari, W. Belzig, A. Leitenstorfer, and D. Brida, Ultrafast pseudospin dynamics in graphene, Phys. Rev. B **92**, 165429 (2015).

[10] J. C. König-Otto, M. Mittendorff, T. Winzer, F. Kadi, E. Malic, A. Knorr, C. Berger, W. A. de Heer, A. Pashkin, H. Schneider, M. Helm, and S. Winnerl, Slow Noncollinear Coulomb Scattering in the Vicinity of the Dirac Point in Graphene, Phys. Rev. Lett. **117**, 087401 (2016).

[11] F. Kadi, T. Winzer, A. Knorr, and E. Malic, Impact of doping on the carrier dynamics in graphene, Sci. Rep. **5**, 16841 (2015).

[12] M. Trushin, Collinear scattering of photoexcited carriers in graphene, Phys. Rev. B **94**, 205306 (2016).

[13] D. Yadav, M. Trushin, and F. Pauly, Photocarrier thermalization bottleneck in graphene, Phys. Rev. B **99**, 155410 (2019).

[14] S. Z. Butler, S. M. Hollen, L. Cao, Y. Cui, J. A. Gupta, H. R. Gutiérrez, T. F. Heinz, S. S. Hong, J. Huang, A. F. Ismach, E. Johnston-Halperin, M. Kuno, V. V. Plashnitsa, R. D. Robinson, R. S. Ruoff, S. Salahuddin, J. Shan, L. Shi, M. G. Spencer, M. Terrones, W. Windl, and J. E. Goldberger, Progress, challenges, and opportunities in two-dimensional materials beyond graphene, ACS Nano **7**, 2898 (2013).

[15] S. Das, J. A. Robinson, M. Dubey, H. Terrones, and M. Terrones, Beyond graphene: Progress in novel two-dimensional materials and van der Waals solids, Annu. Rev. Mater. Res. **45**, 1 (2015).

[16] Q. H. Wang, K. Kalantar-Zadeh, A. Kis, J. N. Coleman, and M. S. Strano, Electronics and optoelectronics of two-dimensional transition metal dichalcogenides, Nat. Nanotechnol. **7**, 699 (2012).

[17] E. N. Voronina, L. S. Novikov, and T. V. Rakhimova, Properties and potential applications of quasi-two-dimensional molybdenum disulfide for nanoelectronic elements, Inorg. Mater.: Appl. Res. **9**, 175 (2018).

[18] M. M. Furchi, A. Pospischil, F. Libisch, J. Burgdörfer, and T. Mueller, Photovoltaic effect in an electrically tunable van der Waals heterojunction, Nano Lett. **14**, 4785 (2014).

[19] L. Britnell, R. M. Ribeiro, A. Eckmann, R. Jalil, B. D. Belle, A. Mishchenko, Y.-J. Kim, R. V. Gorbachev, T. Georgiou, S. V. Morozov, A. N. Grigorenko, A. K. Geim, C. Casiraghi, A. H. Castro Neto, and K. S. Novoselov, Strong light-matter interactions in heterostructures of atomically thin films, Science **340**, 1311 (2013).

[20] W. J. Yu, Y. Liu, H. Zhou, A. Yin, Z. Li, Y. Huang, and X. Duan, Highly efficient gate-tunable photocurrent generation in vertical heterostructures of layered materials, Nat. Nanotechnol. **8**, 952 (2013).

[21] Q. A. Vu, J. H. Lee, V. L. Nguyen, Y. S. Shin, S. C. Lim, K. Lee, J. Heo, S. Park, K. Kim, Y. H. Lee, and W. J. Yu, Tuning carrier tunneling in van der Waals heterostructures for ultrahigh detectivity, Nano Lett. **17**, 453 (2017).

[22] S. Wang, J. Wang, W. Zhao, F. Giustiniano, L. Chu, I. Verzhbitskiy, J. Z. Yong, and G. Eda, Efficient carrier-to-exciton conversion in field emission tunnel diodes based on

MIS-type van der Waals heterostack, Nano Lett. **17**, 5156 (2017).

[23] Z. Nie, R. Long, L. Sun, C.-C. Huang, J. Zhang, Q. Xiong, D. W. Hewak, Z. Shen, O. V. Prezhdo, and Z.-H. Loh, Ultrafast carrier thermalization and cooling dynamics in few-layer MoS_2, ACS Nano **8**, 10931 (2014).

[24] Q. Wang, S. Ge, X. Li, J. Qiu, Y. Ji, J. Feng, and D. Sun, Valley carrier dynamics in monolayer molybdenum disulfide from helicity-resolved ultrafast pump-probe spectroscopy, ACS Nano **7**, 11087 (2013).

[25] H. Shi, R. Yan, S. Bertolazzi, J. Brivio, B. Gao, A. Kis, D. Jena, H. G. Xing, and L. Huang, Exciton dynamics in suspended monolayer and few-layer MoS_2 2D crystals, ACS Nano **7**, 1072 (2013).

[26] D. Sun, Y. Rao, G. A. Reider, G. Chen, Y. You, L. Brézin, A. R. Harutyunyan, and T. F. Heinz, Observation of rapid exciton-exciton annihilation in monolayer molybdenum disulfide, Nano Lett. **14**, 5625 (2014).

[27] Y. Yu, Y. Yu, C. Xu, A. Barrette, K. Gundogdu, and L. Cao, Fundamental limits of exciton-exciton annihilation for light emission in transition metal dichalcogenide monolayers, Phys. Rev. B **93**, 201111(R) (2016).

[28] Q. Cui, F. Ceballos, N. Kumar, and H. Zhao, Transient absorption microscopy of monolayer and bulk WSe_2, ACS Nano **8**, 2970 (2014).

[29] D. Lagarde, L. Bouet, X. Marie, C. R. Zhu, B. L. Liu, T. Amand, P. H. Tan, and B. Urbaszek, Carrier and Polarization Dynamics in Monolayer MoS_2, Phys. Rev. Lett. **112**, 047401 (2014).

[30] H. Wang, C. Zhang, and F. Rana, Ultrafast dynamics of defect-assisted electron-hole recombination in monolayer MoS_2, Nano Lett. **15**, 339 (2015).

[31] T. Yan, S. Yang, D. Li, and X. Cui, Long valley relaxation time of free carriers in monolayer WSe_2, Phys. Rev. B **95**, 241406(R) (2017).

[32] A. Molina-Sánchez, D. Sangalli, L. Wirtz, and A. Marini, *Ab initio* calculations of ultrashort carrier dynamics in two-dimensional materials: Valley depolarization in single-layer WSe_2, Nano Lett. **17**, 4549 (2017).

[33] F. Langer, C. P. Schmid, S. Schlauderer, M. Gmitra, J. Fabian, P. Nagler, C. Schüller, T. Korn, P. G. Hawkins, J. T. Steiner, U. Huttner, S. W. Koch, M. Kira, and R. Huber, Lightwave valleytronics in a monolayer of tungsten diselenide, Nature (London) **557**, 76 (2018).

[34] R. Wang, B. A. Ruzicka, N. Kumar, M. Z. Bellus, H.-Y. Chiu, and H. Zhao, Ultrafast and spatially resolved studies of charge carriers in atomically thin molybdenum disulfide, Phys. Rev. B **86**, 045406 (2012).

[35] L. Wang, C. Xu, M.-Y. Li, L.-J. Li, and Z.-H. Loh, Unraveling spatially heterogeneous ultrafast carrier dynamics of single-layer WSe_2 by femtosecond time-resolved photoemission electron microscopy, Nano Lett. **18**, 5172 (2018).

[36] A. G. Cabo, J. A. Miwa, S. S. Grønborg, J. M. Riley, J. C. Johannsen, C. Cacho, O. Alexander, R. T. Chapman, E. Springate, M. Grioni, J. V. Lauritsen, P. D. C. King, P. Hofmann, and S. Ulstrup, Observation of ultrafast free carrier dynamics in single layer MoS_2, Nano Lett. **15**, 5883 (2015).

[37] G. Moody, C. K. Dass, K. Hao, C.-H. Chen, L.-J. Li, A. Singh, K. Tran, G. Clark, X. Xu, G. Berghäuser, E. Malic, A. Knorr, and X. Li, Intrinsic homogeneous linewidth and broadening mechanisms of excitons in monolayer transition metal dichalcogenides, Nat. Commun. **6**, 8315 (2015).

[38] C. Ruppert, A. Chernikov, H. M. Hill, A. F. Rigosi, and T. F. Heinz, The role of electronic and phononic excitation in the optical response of monolayer WS_2 after ultrafast excitation, Nano Lett. **17**, 644 (2017).

[39] M. Palummo, M. Bernardi, and J. C. Grossman, Exciton radiative lifetimes in two-dimensional transition metal dichalcogenides, Nano Lett. **15**, 2794 (2015).

[40] L. Waldecker, R. Bertoni, H. Hübener, T. Brumme, T. Vasileiadis, D. Zahn, A. Rubio, and R. Ernstorfer, Momentum-Resolved View of Electron-Phonon Coupling in Multilayer WSe_2, Phys. Rev. Lett. **119**, 036803 (2017).

[41] C. J. Ciccarino, T. Christensen, R. Sundararaman, and P. Narang, Dynamics and spin-valley locking effects in monolayer transition metal dichalcogenides, Nano Lett. **18**, 5709 (2018).

[42] M. Bernardi, D. Vigil-Fowler, J. Lischner, J. B. Neaton, and S. G. Louie, *Ab Initio* Study of Hot Carriers in the First Picosecond after Sunlight Absorption in Silicon, Phys. Rev. Lett. **112**, 257402 (2014).

[43] X. Guo, H. Chen, X. Wen, and J. Zheng, Electron-phonon interactions in MoS_2 probed with ultrafast two-dimensional visible/far-infrared spectroscopy, J. Chem. Phys. **142**, 212447 (2015).

[44] M. Bernardi, D. Vigil-Fowler, C. S. Ong, J. B. Neaton, and S. G. Louie, *Ab initio* study of hot electrons in GaAs, Proc. Natl. Acad. Sci. USA **112**, 5291 (2015).

[45] D. Yadav, F. Pauly, and M. Trushin, Charge carrier thermalization in bulk and monolayer CdTe: A first principles study, arXiv:1910.05216.

[46] P. Giannozzi, O. Andreussi, T. Brumme, O. Bunau, M. Buongiorno Nardelli, M. Calandra, R. Car, C. Cavazzoni, D. Ceresoli, M. Cococcioni, N. Colonna, I. Carnimeo, A. Dal Corso, S. de Gironcoli, P. Delugas, R. A. DiStasio, Jr., A. Ferretti, A. Floris, G. Fratesi, G. Fugallo *et al.*, Advanced capabilities for materials modeling with quantum ESPRESSO, J. Phys.: Condens. Matter **29**, 465901 (2017).

[47] N. Troullier and J. L. Martins, Efficient pseudopotentials for plane-wave calculations, Phys. Rev. B **43**, 1993 (1991).

[48] https://dalcorso.github.io/pslibrary/ (accessed on 18.08.2020) .

[49] S. Baroni, S. de Gironcoli, A. D. Corso, and P. Giannozzi, Phonons and related crystal properties from density-functional perturbation theory, Rev. Mod. Phys. **73**, 515 (2001).

[50] N. Marzari, A. A. Mostofi, J. R. Yates, I. Souza, and D. Vanderbilt, Maximally localized Wannier functions: Theory and applications, Rev. Mod. Phys. **84**, 1419 (2012).

[51] F. Giustino, M. L. Cohen, and S. G. Louie, Electron-phonon interaction using Wannier functions, Phys. Rev. B **76**, 165108 (2007).

[52] S. Poncé, E. R. Margine, C. Verdi, and F. Giustino, EPW: Electron-phonon coupling, transport and superconducting properties using maximally localized Wannier functions, Comput. Phys. Commun. **209**, 116 (2016).

[53] R. Coehoorn, C. Haas, J. Dijkstra, C. J. F. Flipse, R. A. de Groot, and A. Wold, Electronic structure of $MoSe_2$, MoS_2, and WSe_2. I. Band-structure calculations and photoelectron spectroscopy, Phys. Rev. B **35**, 6195 (1987).

[54] J. Kang, S. Tongay, J. Zhou, J. Li, and J. Wu, Band offsets and heterostructures of two-dimensional semiconductors, Appl. Phys. Lett. **102**, 012111 (2013).

[55] A. Ramasubramaniam, Large excitonic effects in monolayers of molybdenum and tungsten dichalcogenides, Phys. Rev. B **86**, 115409 (2012).

[56] D. Y. Qiu, F. H. da Jornada, and S. G. Louie, Optical Spectrum of MoS_2: Many-Body Effects and Diversity of Exciton States, Phys. Rev. Lett. **111**, 216805 (2013).

[57] T. Sohier, D. Campi, N. Marzari, and M. Gibertini, Mobility of two-dimensional materials from first principles in an accurate and automated framework, Phys. Rev. Mater. **2**, 114010 (2018).

[58] Y. Ding, Y. Wang, J. Ni, L. Shi, S. Shi, and W. Tang, First principles study of structural, vibrational and electronic properties of graphene-like MX_2 (M = Mo, Nb, W, Ta; X = S, Se, Te) monolayers, Physica B (Amsterdam, Neth.) **406**, 2254 (2011).

[59] A. Molina-Sánchez and L. Wirtz, Phonons in single-layer and few-layer MoS_2 and WS_2, Phys. Rev. B **84**, 155413 (2011).

[60] T. Sohier, M. Gibertini, M. Calandra, F. Mauri, and N. Marzari, Breakdown of optical phonons' splitting in two-dimensional materials, Nano Lett. **17**, 3758 (2017).

[61] F. Giustino, Electron-phonon interactions from first principles, Rev. Mod. Phys. **89**, 015003 (2017).

[62] M. Trushin, Theory of thermionic emission from a two-dimensional conductor and its application to a graphene-semiconductor Schottky junction, Appl. Phys. Lett. **112**, 171109 (2018).

[63] L. D. Landau and E. M. Lifshitz, *Quantum Mechanics: Non-Relativistic Theory* (Butterworth-Heinemann, Oxford, 2004) .

[64] E. Linardy, M. Trushin, K. Watanabe, T. Taniguchi, and G. Eda, Electro-optic upconversion in van der Waals heterostructures via nonequilibrium photocarrier tunneling, Adv. Mater. **32**, 2001543 (2020).

[65] J. Sjakste, N. Vast, M. Calandra, and F. Mauri, Wannier interpolation of the electron-phonon matrix elements in polar semiconductors: Polar-optical coupling in GaAs, Phys. Rev. B **92**, 054307 (2015).

[66] T. Sohier, M. Calandra, and F. Mauri, Two-dimensional Fröhlich interaction in transition-metal dichalcogenide monolayers: Theoretical modeling and first-principles calculations, Phys. Rev. B **94**, 085415 (2016).

[67] L. Wang, Z. Wang, H.-Y. Wang, G. Grinblat, Y.-L. Huang, D. Wang, X.-H. Ye, X.-B. Li, Q. Bao, A.-S. Wee, S. A. Maier, Q.-D. Chen, M.-L. Zhong, C.-W. Qiu, and H.-B. Sun, Slow cooling and efficient extraction of C-exciton hot carriers in MoS_2 monolayer, Nat. Commun. **8**, 13906 (2017).